Enhanced visible light photocatalytic water reduction from a g-C₃N₄/SrTa₂O₆ heterojunction

Shiba P. Adhikari [a,b], Zachary D. Hood [c,d], Hui Wang [c,e], Rui Peng [c], Alex Krall [a], Hui Li [a], Vincent W. Chen [d], Karren L. More [c], Zili Wu [c], Scott Geyer [a], Abdou Lachgar [a,b,*]

[a] Department of Chemistry, Wake Forest University, Winston-Salem, NC, 27109, USA
[b] Center for Energy, Environment and Sustainability (CEES), Wake Forest University, Winston-Salem, NC, 27109, USA
[c] Center for Nanophase Materials Sciences, Oak Ridge National Laboratory, Oak Ridge, TN, 37831, USA
[d] School of Chemistry and Biochemistry, Georgia Institute of Technology, Atlanta, GA, 30332, USA
[e] Department of Mechanical Engineering, Conn Center for Renewable Energy Research, University of Louisville, KY, 40292, USA

ABSTRACT

A new g-C₃N₄/SrTa₂O₆ heterojunction photocatalyst was designed and prepared by *chimie douce* (soft chemistry) method where carbon nitride (g-C₃N₄) was deposited over the metastable perovskite phase of SrTa₂O₆. The morphological study of the heterojunction using SEM and STEM revealed that g-C₃N₄ nanofibers are dispersed uniformly on the surface of SrTa₂O₆ plates leading to the intimate contact between them. The heterojunction could achieve a high and stable visible light photocatalytic H₂ generation of 137 mmol/h/mole of g-C₃N₄, which is much larger than the amount of hydrogen generated by one mole of pristine g-C₃N₄. A plausible mechanism for the observed enhanced photocatalytic activity for the heterojunction is proposed on the basis of effective charge separation of photogenerated electron-hole pairs, supported by band position calculations and photo-physical properties of g-C₃N₄ and SrTa₂O₆.

© 2017 Elsevier B.V. All rights reserved.

1. Introduction

Semiconductor-based heterogeneous photocatalysis is considered as one of the most important green technologies capable of converting solar energy into chemically stored energy. The discovery of photoelectrochemical splitting of water by n-TiO₂ electrodes in the 1970s led to the study and development of numerous semiconductor-based photocatalysts including oxides, sulfides, and oxynitrides for solar fuels generation and environmental remediation [1–4]. However, most of these photocatalysts require ultraviolet (UV) light to generate electron-hole pairs, necessary for electrochemical processes at the surface of the semiconductors. An optimal photocatalyst should be: (i) active under visible light to maximize the use of solar spectrum, which consists of ~4% UV, ~45% visible, and ~50% infrared light, (ii) chemically and photo stable, and (iii) readily available and inexpensive [5,6]. In addition, for a photocatalyst to be active efficiently towards specific electrochemical processes, the position of its valence band (VB) and conduction band (CB) should be appropriately located [7,8]. For instance, for the photo-reduction of water to produce hydrogen, the bottom of the CB must be located at energy levels lower than 0 eV (*i.e.* H⁺/H₂ energy level in NHE scale).

Band gap engineering is a common approach to extend the absorption range of UV active materials towards visible light region [9,10]. Besides doping with an anion, and/or a cation, great efforts have been made to design semiconductor heterojunctions by coupling a UV-active semiconductor with a second material (either a dye or another semiconductor) [11–13]. In addition to the extension of light absorption range towards the visible light region, properly designed heterojunctions can also lead to separation of photogenerated charge carriers, thus increasing their lifetime and allow them to participate in surface electrochemical processes [14–16].
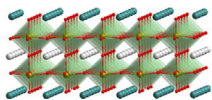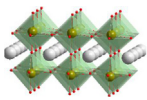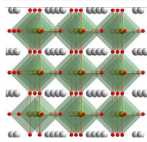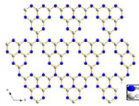
Layered perovskites possess a wide variety of properties, such as chemical intercalation, ionic exchange, electron transport and excellent catalytic activities [17,18]. They consist of two-dimensional perovskite slabs interleaved with cations or cationic structural units [19]. A number of layered perovskites were investigated for their photocatalytic properties due to the possibility of modulating their physical properties by modifying their chemical composition and their structure by means of

* Corresponding author at: Department of Chemistry, Wake Forest University, Winston-Salem, NC, 27109, USA.
  E-mail address: lachgar@wfu.edu (A. Lachgar).

Table 1
Crystal structure representations and parameters of photocatalysts in this study.

Compounds	KSTO	HSTO	STO	CN
Crystal structure representation				
Crystal structure parameters	*I4/mmm* *a = 3.976(2)* Å, *c = 21.711(5)* Å	*P4/mmm* *a = 3.869(9)* Å, *c = 9.652(4)* Å	*Pm 3̄ m* *a = 3.943(2)* Å	*P6̄* *a = 6.508(7)* Å, *c = 6.695(2)* Å

ion-exchange, intercalation, or pillaring. Among different types of layered perovskite, Ruddlesden-Popper (RP) phases consist of two-dimensional anionic perovskite slabs held together by cations [20]. $A_2SrTa_2O_7$ (A = H, Li, K, and Rb)-type tantalates are new members of the RP-type layered perovskite composed of $\{SrTa_2O_7\}^{2-}_{\infty}$ perovskite sheets held together by Li⁺, K⁺, Rb⁺, or H_3O^+ [21–23]. The layered acid phase converts to metastable three-dimensional cubic perovskite $SrTa_2O_6$ that can be isolated only through *chimie douce* synthesis method.

The recent discovery of graphitic carbon nitride (g-C_3N_4) as visible-light active photocatalyst has attracted tremendous attention in the last few years due to its layered structure, and its high chemical stability in aqueous solutions over a broad pH range [24]. Its relatively small band gap (~2.7 eV) makes it promising for large-scale photocatalytic applications [25]. Nevertheless, g-C_3N_4 suffers from shortcomings such as rapid recombination of photo-generated electron–hole pairs and relatively small surface area [26,27]. To overcome these drawbacks, several strategies, including elemental dopings with sulfur or phosphorus [28,29], engineering mesoporous structure [30–33], and coupling with other semiconductors to form heterojunctions, were used. In the context of heterojunction formation, the two-dimensional layered structure of g-C_3N_4 similar to graphene is amenable to hybridization with other components to form different heterojunctions. Several g-C_3N_4-based heterojunctions have been synthesized and displayed significantly higher photocatalytic activity under visible light irradiation [34,35].

We recently reported the synthesis, characterization, and photocatalytic activity of g-C_3N_4/$Sr_2Nb_2O_7$ heterojunction [36]. The incorporation of g-C_3N_4 in $Sr_2Nb_2O_7$ not only extends light absorption range of $Sr_2Nb_2O_7$ but more importantly, dramatically enhances the photocatalytic activity of g-C_3N_4. We showed how proper selection of materials and proper synthetic techniques to chemically form genuine and stable heterojunctions can lead to remarkably enhanced photocatalytic activity. Here, we report results of a study in which we extended our scope to *in situ* synthesis of a heterojunction in which one component is a metastable oxide. Thermal condensation of melamine in the presence of $H_2SrTa_2O_7$ led to the formation of g-C_3N_4/$SrTa_2O_6$ (CN/STO) heterojunction. Metastable oxide ($SrTa_2O_6$) was formed during dehydration/condensation of $H_2SrTa_2O_7$. Thus, CN/STO heterojunction was synthesized *in situ* at relatively low temperatures using so-called "**chimie douce**" method, previously applied to the synthesis of metastable oxides as reported by Oliver and Mallouk [37]. In addition to the photocatalytic study of CN/STO heterojunction, we also performed a comprehensive study of $K_2SrTa_2O_7$ (KSTO), its proton exchanged form, $H_2SrTa_2O_7$ (HSTO), and the metastable perovskite, $SrTa_2O_6$ (STO). The crystal structure representation along with refined unit cell parameters of KSTO, HSTO, STO, and CN are presented in Table 1. The photocatalysts studied were characterized by a variety of techniques, and their photocatalytic performances in the reduction of water under visible and UV light irradiation were evaluated. The CN/STO heterojunction was

found to exhibit remarkably enhanced the photocatalytic generation of H_2 under visible light irradiation.

2. Experimental section

2.1. Synthesis

2.1.1. Preparation of $K_2SrTa_2O_7$ (KSTO) and hydrated KSTO

The compound $K_2SrTa_2O_7$ was synthesized by a high-temperature solid-state reaction using potassium citrate ($K_3C_6H_5O_7 \cdot H_2O$, Fisher Scientific, 99.0%), strontium nitrate ($Sr(NO_3)_2$, Alfa Aesar, 99%) and tantalum oxide (Ta_2O_5, Alfa Aesar, 99.95%) as precursors. In a typical synthesis, 5 mmol of each precursor (33% molar excess $K_3C_6H_5O_7 \cdot H_2O$) were ground together in an agate mortar to form a homogeneous powder, then transferred to an alumina crucible, and heated to 500 °C at the rate of 2 °C/min. The temperature was maintained at 500 °C for 4 h to decompose the citrate precursors, then cooled to room temperature. The product was ground again to obtain a fine white powder, then transferred back to an alumina crucible and heated to 1000 °C at a rate of 10 °C/minute and held at this temperature for 12 h, then cooled to room temperature to obtain a white microcrystalline powder, which was confirmed to be anhydrous $K_2SrTa_2O_7$ by PXRD. The anhydrous phase is spontaneously hydrated to form $K_2SrTa_2O_7 \cdot 0.92H_2O$ upon exposure to air for 48 h or washing with water, as previously reported in the literature [21,22,37]. The number of water molecules per formula unit was determined by TGA.

2.1.2. Preparation of $H_2SrTa_2O_7$ (HSTO)

The acid form $H_2SrTa_2O_7$ was obtained by ion exchange of $K_2SrTa_2O_7$ using 4 M HNO_3 aqueous solution. In a typical experiment, 2.00 g of $K_2SrTa_2O_7$ was added to 250 mL 4 M HNO_3 at room temperature and stirred for 4 days. The acid solution was refreshed twice during this period. The white solid, $H_2SrTa_2O_7$ was isolated by filtration, and washed with deionized water, then dried under vacuum at 25 °C for 6 h. Complete exchange of K⁺ ions with protons was confirmed by induced coupled plasma optical emission spectroscopy (ICP-OES) analysis.

2.1.3. Preparation of g-C_3N_4/$SrTa_2O_6$ (CN/STO) heterojunction, pristine g-C_3N_4 (CN), and $SrTa_2O_6$ (STO)

The heterojunction, g-C_3N_4/$SrTa_2O_6$ (CN/STO), was synthesized by thermal decomposition of melamine ($C_3H_6N_6$, Sigma-Aldrich, 99.0%) in the presence of $H_2SrTa_2O_7$. In a typical reaction, 1.000 g of HSTO was added to 50 mL of water containing 5.000 g of melamine (the 1:5 HSTO: Melamine mass ratio was determined from optimization experiments done to determine the best performing heterojunction, Fig. S12, ESI). The mixture was sonicated for 15 min, stirred for 30 min, then transferred to a Teflon-lined stainless steel autoclave, sealed, and heated at 200 °C for 24 h under autogenous pressure. The product was filtered and washed twice with water to obtain a white microcrystalline powder. The white powder was

calcined at 550 °C for 4 h to obtain a yellow colored powder, which was confirmed by PXRD to be the g-C$_3$N$_4$/SrTa$_2$O$_6$ (CN/STO) heterojunction. During the calcination process, H$_2$SrTa$_2$O$_7$ was converted to the metastable perovskite phase of SrTa$_2$O$_6$. Pure g-C$_3$N$_4$ (CN) was synthesized by following the same two-step method. In a typical reaction, 5.000 g of melamine was dispersed in 50 mL of water by sonication and stirring. The dispersed solution was hydrothermally treated at 200 °C for 24 h before calcining at 550 °C for four hours. Pure SrTa$_2$O$_6$ (STO) was synthesized by calcining HSTO at 550 °C for 4 h.

2.2. Characterization

Powder X-ray diffraction (PXRD) measurements were collected on a Bruker-D2 Phaser diffractometer equipped with Cu-Kα radiation (λ = 0.15418 nm) at an operating voltage of 30 kV and current of 10 mA. The microstructure and elemental mapping were performed on a scanning transmission electron microscope (STEM, Hitachi HF3300) at 300 kV equipped with a Bruker silicon drift detector (SDD). Scanning electron microscopy (SEM) images were collected on a Zeiss Merlin FE-SEM with an operating voltage at 5.0 kV and further EDS elemental mappings were completed on an energy dispersive spectrometer (Bruker) at 10.0 kV. Differential scanning calorimetry (DSC) and thermogravimetric analysis (TGA) were completed using an SDT-Q600 (TA Instruments, USA) under constant airflow (100 mL/min) and a heating rate of 10 °C/min. X-ray photoelectron spectroscopy (XPS) was performed using a Kratos Axis Ultra DLD X-ray photoelectron spectrometer. The samples were analyzed as powders mounted on small pieces of indium metal. Surface areas were determined from nitrogen adsorption isotherms at 77 K by applying Brunauer-Emmett-Teller (BET) equation, using Autosorb-iQ from Quantachrome. Diffuse reflectance UV–vis spectra (DRS) were collected on an Ocean Optics FLAME-S-XR1-ES spectrophotometer equipped with an integrating sphere. Fourier transform infrared spectra (FTIR) were recorded on a Spectrum 100 spectrometer (PerkinElmer). Photoluminescence (PL) and time-resolved fluorescence emission decay measurements were collected on a Horiba JobinYvon Fluorolog Fluorimeter (Model No. FL-1057) using a 450 W Xe lamp/monochromator combination and a pulsed LED (Model NanoLED N-330), respectively, as the excitation sources. The excitation monochromator was set at 336 nm to match the pulsed LED's output for both emission and lifetime measurements. The microcrystalline samples were packed in the well of the sample holder (Model No. 1933) oriented at 60° relative to the excitation source to minimize scattering. All measurements were performed at room temperature. The emission signals best fit tri-exponential decay kinetics rather than mono-, bi- or tetra-exponential kinetics. The average lifetime (τ$_{avg}$) was determined by the following equation:

$$\tau_{avg} = \frac{\sum A_i \tau_i^2}{\sum A_i \tau_i}$$

where A$_i$ and τ$_i$ are the amplitudes (or weighting factors), and lifetimes, respectively.

Electrochemical impedance spectroscopy (EIS) was measured with a Gamry 3000 electrochemical workstation. Spectra were collected using a conventional three-electrode system consisting of fluorine-doped tin oxide (FTO) as the working electrode, Ag/AgCl as the reference electrode, and platinum wire as the counter electrode. The measurements were performed using a 5.0 mV AC voltage signal at 1 V vs Ag/AgCl between 100 kHz–0.1 Hz in 0.5 M Na$_2$SO$_4$ solution. The working electrode was prepared by spin coating a slurry of photocatalyst on FTO glass (dimensions: 1 cm × 1 cm), and drying in an oven at 60 °C.

2.3. Photocatalytic performance

Photocatalytic studies were carried out in a Pyrex reaction vessel (80 mL capacity) connected to a closed gas circulation system. A 300 W Xenon lamp (Newport Corporation) was used as the light source with a 420 nm cut-off filter to provide visible light irradiation. All experiments were performed at ambient temperature (25 °C). In a typical photocatalytic reaction, 50 mg of photocatalyst was dispersed in 50 mL of deionized water containing 5% of triethanolamine used as a hole scavenger. The suspension was degassed with N$_2$ gas for 30 min and then exposed to visible light irradiation (λ ≥ 420 nm) under magnetic stirring. For water-splitting experiments, 50 mL of deionized water was used without addition of cocatalyst or hole scavengers. The amount of hydrogen or oxygen produced was quantified by gas chromatography using an HP 6890 GC equipped with TCD, with argon as a carrier gas. To study the stability and recyclability of the CN/STO heterojunction the suspension of the photocatalyst was degassed at the end of each cycle for 30 min using nitrogen gas. When a cocatalyst was used, Pt co-catalyst (2.5% by weight) was deposited using the photo-deposition method where chloroplatinic acid hexahydrate (H$_2$PtCl$_6$·6H$_2$O, Sigma-Aldrich) was used as the Pt source. In a typical reaction of co-catalyst loading, 50 mg of the photocatalyst and 3.31 mg of chloroplatinic acid hexahydrate were introduced into a pyrex photocatalytic cell with 50 mL of aqueous solution containing 5 mL of methanol. The suspension was irradiated with UV light for 4 h with constant magnetic stirring. The gray colored Pt coated samples were recovered using centrifugation and dried in vacuum at 60 °C for 4 h. The apparent quantum yield (AQY) was calculated using equation.

$$AQY(\%) = \frac{\text{number of evolved H}_2 \text{ molecules} \times 2}{\text{number of incident photons}} \times 100$$

The average irradiation intensity (λ = 420 nm) was determined to be 0.45 W/cm^2 with irradiation area of 4.12 cm^2. The number of incident photons (N) was calculated to be 2.80×10^{21} for one hour of irradiation. Similarly, the turnover number and turnover frequencies were calculated using equations:

$$TON = \frac{\text{number of moles of H}_2 \text{ evolved}}{\text{number of moles of CN on the photocatalyst}}$$

$$TOF = \frac{TON}{\text{Reaction time (hours)}}$$

3. Results and discussions

3.1. Synthesis

A **chimie douce** (soft chemistry) method was used to synthesize the CN/STO heterojunction by depositing CN over STO as shown in Scheme 1.

The K$_2$SrTa$_2$O$_7$ precursor was first synthesized using high-temperature solid-state reaction by heating a mixture of potassium citrate, strontium nitrate, and tantalum oxide. The acid form, H$_2$SrTa$_2$O$_7$, was obtained by ion exchange using aqueous nitric acid. For the preparation of heterojunction, the proton exchanged form was homogenously mixed with melamine and subjected to hydrothermal treatment. The product of the hydrothermal treatment was then heated at 550 °C to form g-C$_3$N$_4$ nanofibres anchored to the cubic phase of SrTa$_2$O$_6$ obtained from dehydration of H$_2$SrTa$_2$O$_7$.

3.2. Characterization

The PXRD patterns of the samples studied are shown in Fig. 1a. The pattern of KSTO obtained immediately after synthesis corre-
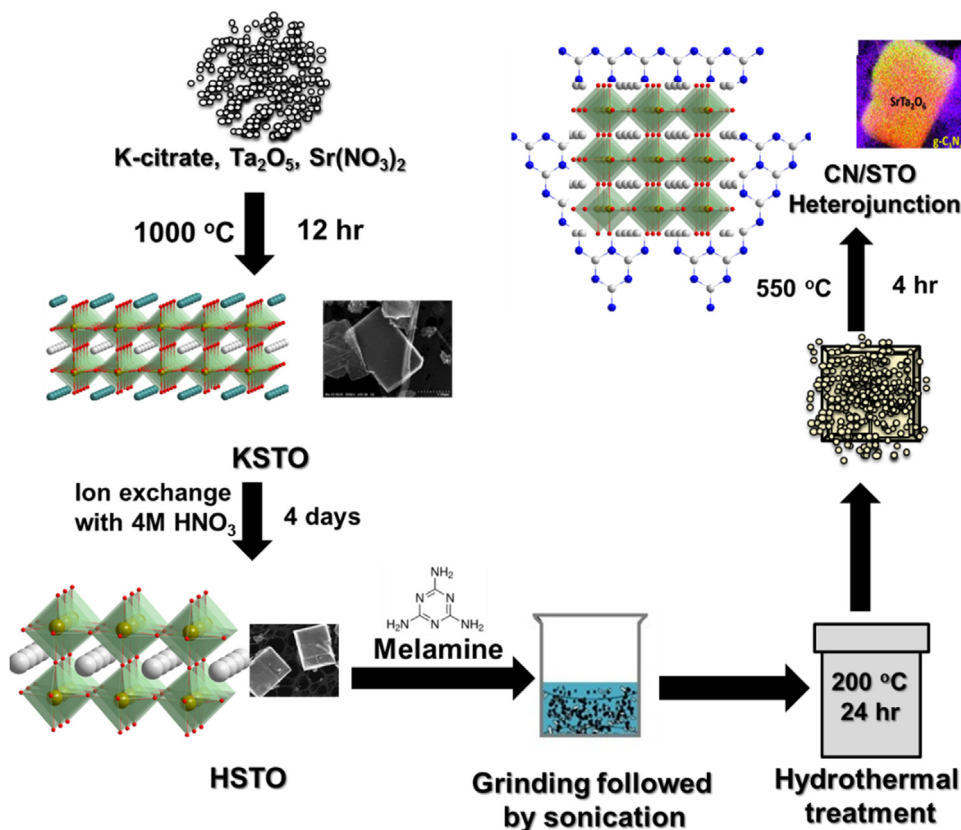
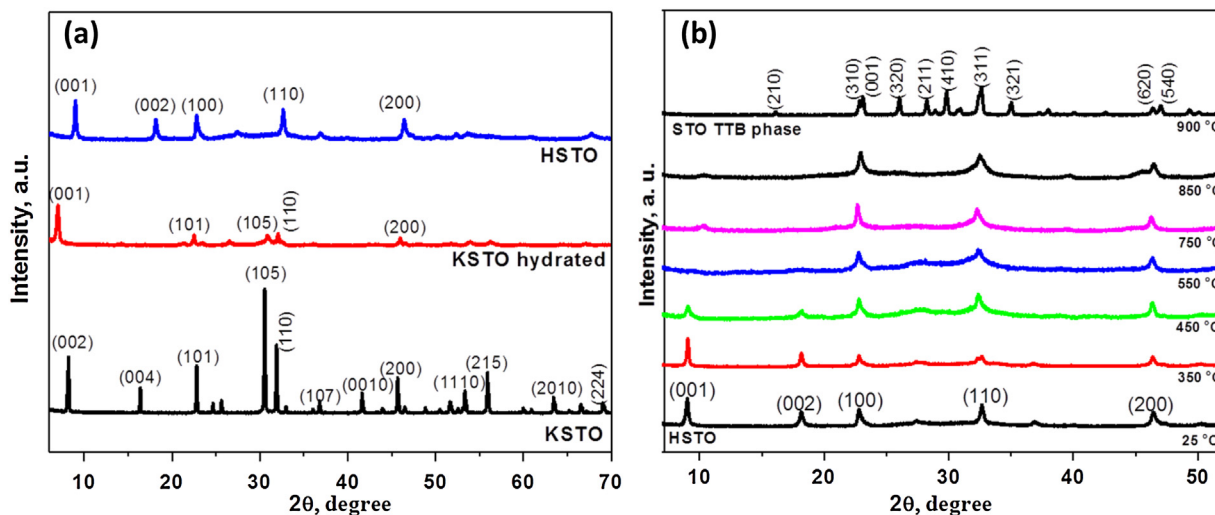**Scheme 1.** Schematic diagram of synthesis of CN/STO heterojunction.

Fig. 1. (a) PXRD of KSTO, hydrated KSTO, and HSTO. (b) Changes in PXRD patterns of HSTO heated at different temperatures.

sponds to that of the anhydrous phase. The pattern was indexed in a tetragonal cell, ($I4/mmm$, $a = 3.976(2)$ Å, $c = 21.711(5)$ Å). These values are consistent with the reported values [21,37]. The anhydrous form converts to the hydrated form upon exposure to air or washing with water (Fig. 1a). The structural change due to hydration is commonly observed in layered perovskites [21,22,37]. The conversion to $K_2SrTa_2O_7 \cdot nH_2O$ is complete after 48 h of air exposure (Fig. S1, ESI). Thermogravimetric and differential scanning calorimetry (TGA/DSC) analysis of $K_2SrTa_2O_7 \cdot nH_2O$ shows a distinct loss of water in the temperature range 60 °C < T < 150 °C (Fig. S2, ESI). The chemical formula of hydrated KSTO was estimated from the TGA to

be $K_2SrTa_2O_7 \cdot 0.92H_2O$, close to the formula reported by Shimizu et al. [38].

The PXRD pattern of hydrated KSTO (Fig. 1a) was indexed in a primitive tetragonal unit cell ($P4/mmm$, $a = 3.946(5)$ Å, and $c = 12.133(7)$ Å). Adjacent layers are stacked immediately above each other leading to halving the c-axis upon hydration. During the hydration, the most prominent change in the PXRD patterns was observed in the (001) reflections, which shifted to lower 2θ values with some peak broadening [21]. PXRD of the acid $H_2SrTa_2O_7 \cdot nH_2O$ (HSTO) shown in Fig. 1a, is also consistent with previously reported patterns [37,39]. All observed diffraction peaks could be indexed
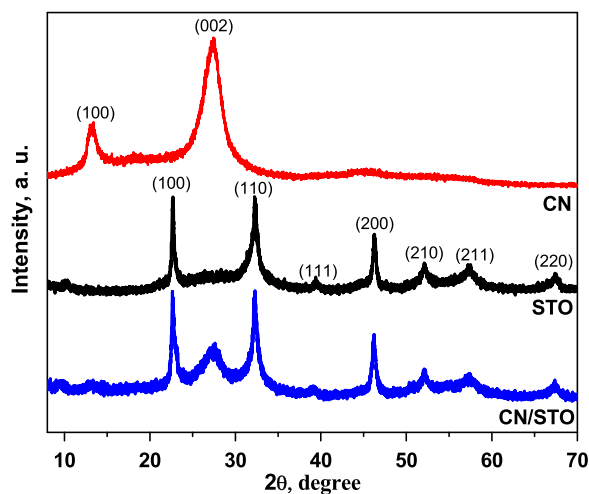
Fig. 2. PXRD of STO, CN and CN/STO heterojunction.

in a primitive tetragonal unit cell (*P4/mmm, a = 3.869(9)* Å, *and c = 9.652(4)* Å). TGA/DSC analysis of HSTO exhibits multistep weight loss up to ~550 °C (Fig. S3, ESI). The number of water molecules per formula unit was determined to be 0.6 (Fig. S3, ESI). PXRD at various temperatures (Fig. 1b) indicate no noticeable structural changes up to 350 °C. After 350 °C, the compound converts to the metastable cubic phase of $SrTa_2O_6$ (STO). The conversion is complete at 550 °C as confirmed by PXRD. This structural change was previously reported by Mallouk et al. [37]. The cubic STO is stable up to 850 °C, when the tetragonal tungsten bronze (TTB) phase of $SrTa_2O_6$ forms [22].

The g-C_3N_4/$SrTa_2O_6$ (CN/STO) heterojunction was fabricated *in situ* by thermal decomposition of melamine in the presence of HSTO. The presence of the two components was confirmed by PXRD (Fig. 2). The diffraction peaks observed at $2\theta = 13.0°$ and $27.3°$ correspond to (100) and (002) diffraction planes of CN (JCPDS 87-1526) [30,40]. Similarly, the diffraction peaks of STO synthesized *in situ* during thermal decomposition of melamine to form CN, were indexed in cubic perovskite phase (*Pm$\bar{3}$m, a = 3.943(2)* Å), and is isostructural with $CaTa_2O_6$ [37,41]. The presence of g-C_3N_4 in the CN/STO heterostructure was further confirmed by the Fourier transform infrared (FTIR) spectroscopy (Fig. S4, ESI).

To better follow the phase formation that occurs during the synthesis of CN/STO heterojunction, PXRD was obtained at various temperatures (Fig. S5, ESI). The PXRD at 25 °C corresponds to that of crystalline product obtained after hydrothermal treatment of melamine in the presence of HSTO. The diffraction peaks of HSTO are clearly visible, which indicates that the hydrothermal step does not change the HSTO pattern. As the mixture is heated, the intensity of the peaks of HSTO decreases, and completely disappear after 350 °C. The other peaks observed at low temperatures (25 °C, 350 °C, and 450 °C) are from the hydrothermal treatment of melamine [42]. As the intensity of the peaks of HSTO decreases, the peaks of cubic STO appear indicating a complete transformation of HSTO to STO. The broad peak of CN observed around 25–30° at 550 °C disappears after 650 °C indicating complete oxidation of CN. The PXRD study indicates that the cubic perovskite STO is completely converted to the tetragonal tungsten bronze phase of $SrTa_2O_6$ (STO-TTB) when heated to temperatures >900 °C.

TGA/DSC of the CN/STO heterojunction (Fig. S6a, ESI) shows a small weight loss (~1%) before 120 °C, which may be due to the removal of surface adsorbed water molecules. The major weight loss (~51%) observed at ~550 °C corresponds to the decomposition of carbon nitride. The DSC study shows one major endothermic peaks at 595 °C, which corresponds to the decomposition of carbon

nitride. This result is further supported by the TGA/DSC of pristine CN sample shown in Fig. S6b, ESI. TGA data also confirms the 1:1 mass ratio of CN and STO in the heterojunction. The same mass ratio was used to prepare a heterogeneous blend sample of CN and STO (for comparative photocatalytic activity study).

The microstructure and surface morphology of KSTO, HSTO, STO, CN and CN/STO heterojunction were investigated using scanning electron microscopy (SEM) (Fig. 3). Crystallites of KSTO, HSTO, and STO possess rectangular sheet-like shapes with side length in the micrometer range and thickness of 100–150 nm. STO sample contains different rectangular plates with different dimensions as shown in Fig. S7, ESI. Crystals of tungsten bronze STO obtained after heating HSTO at 900 °C maintain the plate-like morphology (Fig. S8, ESI). In this study, CN crystallites are shaped as fibers consistent with similar samples synthesized by two-step thermal condensation of melamine as reported by Jin et al. [42]. Images of CN/STO heterojunction show rectangular plates of STO uniformly covered with CN fibers, with intimate contact between CN and STO. This conclusion was further supported by EDS elemental mapping of CN/STO, which shows the homogeneous distribution of nitrogen, strontium, and tantalum (Fig. 3f–i). Additional STEM images for CN/STO are givne in Fig. S9 (ESI).

The microstructure of CN/STO heterojunction was further investigated by high-resolution STEM (Fig. 4), which revealed that CN displays an aggregated fiber-like morphology (Fig. 4a), while STO consists of micrometric plate-like crystals (Fig. 4b). Most STO plates are randomly covered by fibre-like CN particles (Fig. 4c), leading to the formation of CN/STO heterostructured material. Elemental mapping of the CN/STO heterojunction (Fig. 4d) shows the homogeneous distribution of Ta and Sr in the STO plate surrounded by CN.

Diffuse reflectance UV–vis spectra of all materials studied are shown in Fig. 5a. KSTO, HSTO, and STO have an absorption band in the ultraviolet region with a clear absorption edge at ~312–320 nm. The CN/STO heterojunction shows stronger absorbance at a wavelength higher than 450 nm. Optical band gap energies determined by diffuse reflectance UV–vis indicating a red shift of *Eg* toward the visible region when CN is coupled with STO. The band gaps were determined by fitting the absorption spectra with the following Eq. (1) [43]:

$$\alpha h\nu = A(h\nu - Eg)^{n/2} \tag{1}$$

where α, *h*, ν, *A*, and *Eg* are the absorption coefficient, Plancks' constant, light frequency, proportionality constant, and band gap energy, respectively; *n* corresponds to the electronic transition properties of the semiconductor (*n* = 1 for a direct band-gap transition and *n* = 4 for an indirect band gap transition). KSTO, HSTO, and STO were assumed to be direct band gap semiconductors (*n* = 1), while CN is an indirect band gap semiconductor (*n* = 4) [36,44,45]. The optical band gaps of STO and CN were estimated to be 3.94 eV and 2.74 eV, respectively (Fig. 5b). Similarly, the band gap values for KSTO and HSTO were calculated to be 3.92 and 3.96 eV, respectively.

The chemical composition and metal oxidation states were further investigated by X-ray photoelectron spectroscopy (XPS). Fig. 6a shows the survey scan XPS spectra for STO, CN, and the CN/STO which indicate that CN/STO is composed of C, N, Sr, Ta and O elements. Similarly, survey scans of KSTO and HSTO are shown in Fig. S10, ESI. The binding energies obtained from XPS data are summarized in Table 2. High-resolution XPS data of C 1s (Fig. 6b) in CN showed a major peak at 288.1 eV, associated with sp^2 hybridized carbon from the aromatic groups. A small peak around 284 eV corresponds to C—C and/or adventitious carbon [46]. The N 1s peak was observed at 398.47 eV for CN (Fig. 6c). C 1s and N 1s peaks for the heterojunction are observed at slightly lower binding energy values than in pristine CN. The shift to lower energy can be attributed to the relatively strong interaction between CN and STO in the het-
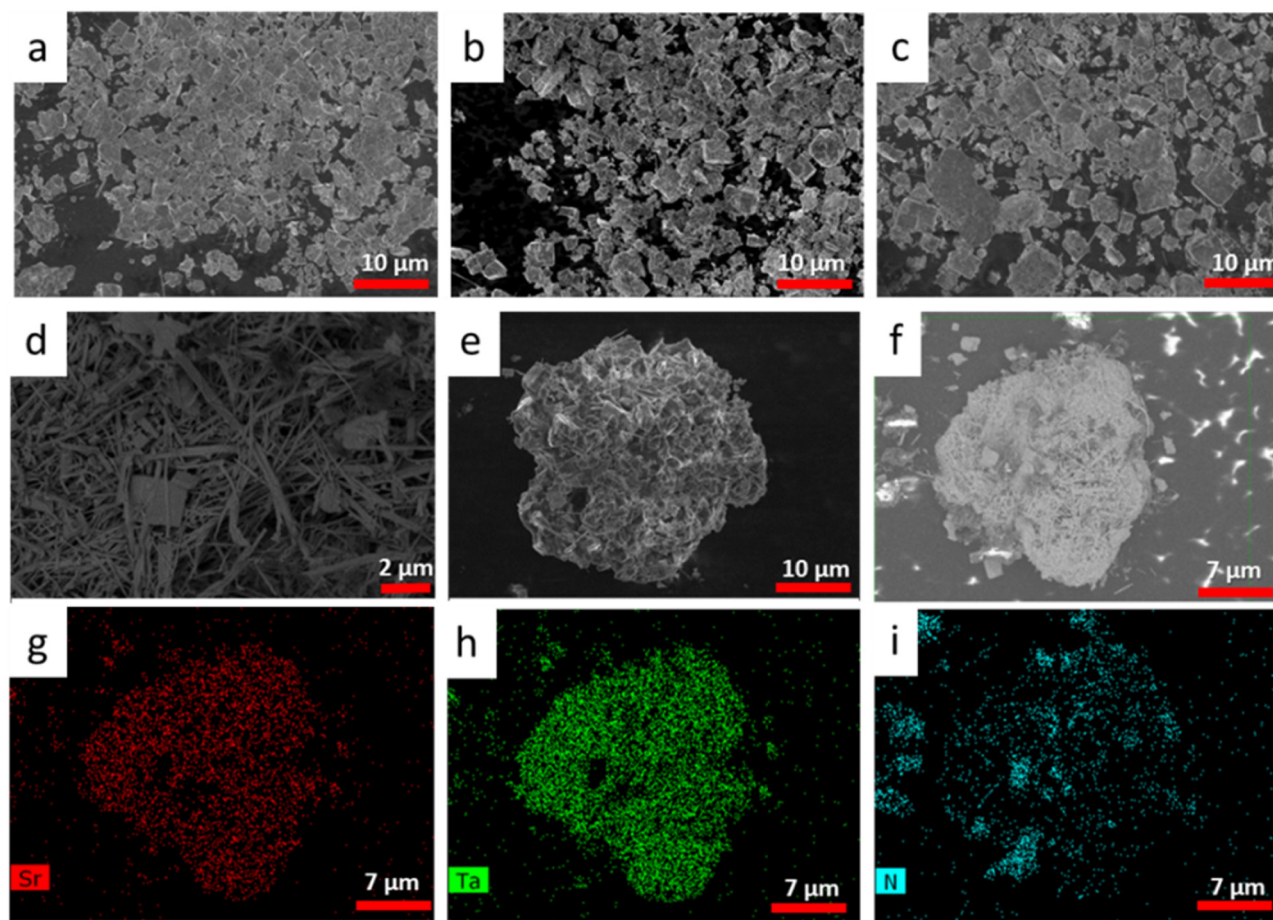
Fig. 3. SEM images for (a) KSTO, (b) HSTO, (c) STO, (d) CN, (e, and f) CN/STO heterojunction. (g–i) are the elemental mappings for Sr, Ta, and N in the image (f).

Table 2
Binding energy values for C 1s, N 1s, Sr 3d, Nb 3d and O 1s in CN, STO, and CN/STO samples.

Sample	Binding Energy Values, eV					
	C 1s	N 1s	Sr 3d	O 1s	Ta 4f	K 2p
KSTO	–	–	132.86 134.60	530.27	25.78	296.79
HSTO	–	–	132.95 134.38	530.28	25.89	–
CN	287.90	398.47	–	–	–	–
STO	–	–	132.82 134.73	530.16	25.78	–
CN/STO	287.45	398.01	131.76 134.60	530.01	25.19	–

erojunction [47–49]. Similar shifts were also observed for Sr 3d and Ta 4f peaks (Fig. S11, ESI).

3.3. Photocatalytic performance

The photocatalytic performance was examined for water splitting under visible and/or UV light irradiation. To determine the optimal CN/STO mass ratio, heterojunctions with different CN/STO ratios were fabricated, and their photocatalytic activities were determined by measuring the amount of hydrogen generated from water reduction under visible light ($\lambda \geq 420$ nm) irradiation. The heterojunction with 1:1 mass ratio (as confirmed by TGA/DSC, Fig. S6a, ESI) was found to have the best performance for hydrogen generation under visible light irradiation (Fig. S12, ESI) and was used throughout this study.

The overall water splitting ability of the catalysts studied are summarized in Table S1, ESI. In a typical experiment, 50 mg of catalyst was suspended in 50 mL of deionized water (without cocatalyst or hole scavenger). Under UV light irradiation,

the amounts of hydrogen and oxygen produced by KSTO were found to be 37.5 µmol/h and 16.5 µmol/h respectively. Similarly, HSTO produced 36.0 µmol/h and 17.0 µmol/h of H_2 and O_2 under UV light irradiation. The study showed that the tantalum-based Ruddlesden-Popper–type perovskite is capable of splitting water into hydrogen and oxygen in 2 to 1 ratio under UV light irradiation. In contrast, cubic STO obtained from dehydration of HSTO showed minimal activity. This result could be due to loss of the layered structure during the formation of three-dimensional metastable phase. The water splitting capacity of CN was found to be negligible, as no oxygen was observed under UV nor under visible light irradiation, which suggests a high recombination rate of photogenerated electron/hole pairs. The study also revealed that under UV light the CN/STO heterojunction showed some hydrogen and oxygen production while no oxygen and only trace amounts of hydrogen were observed under visible light irradiation.

The photocatalytic activities using platinum cocatalyst and hole scavengers were also performed for all catalysts. The amount of hydrogen generated from photocatalytic water reduction was
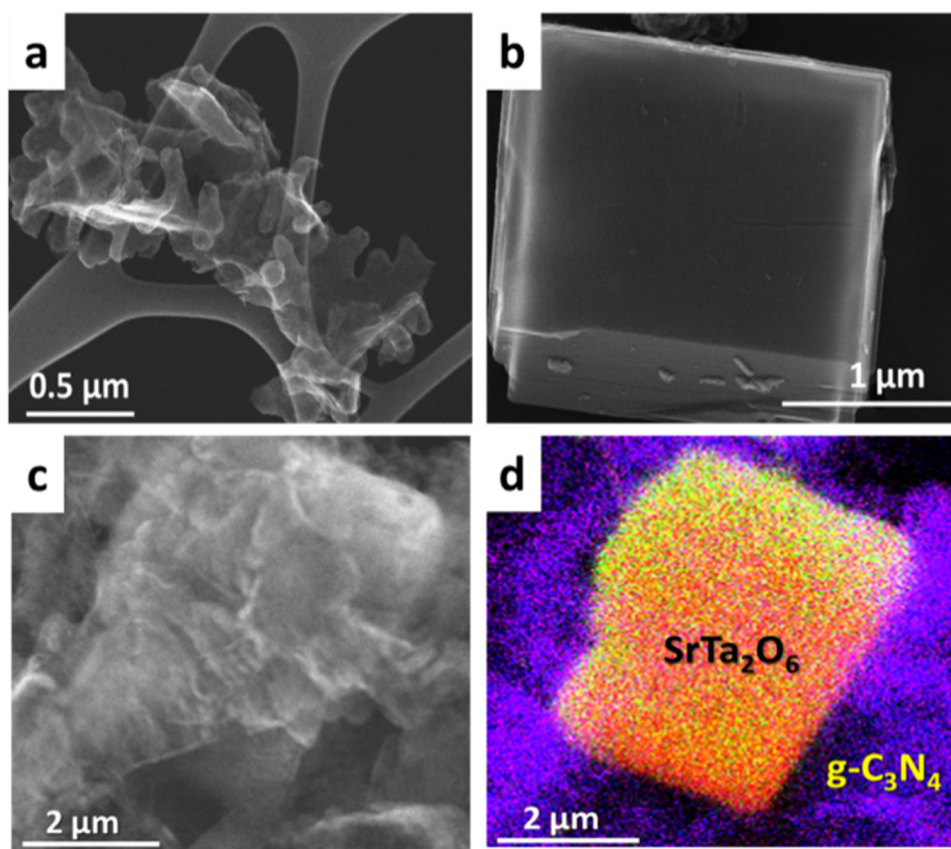
Fig. 4. STEM images for (a) CN, (b) STO and (c, and d) CN/STO heterojunction. Color codes for EDS mapping in (d): N (purple), Ta (yellow), Sr (pink). (For interpretation of the references to colour in this figure legend, the reader is referred to the web version of this article.)
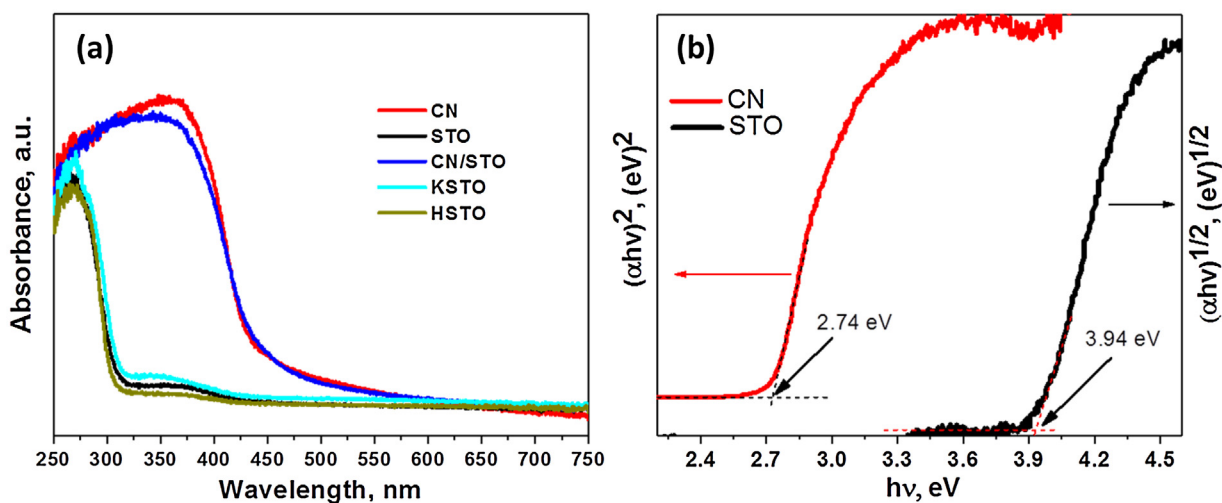

Fig. 5. (a) Diffuse reflectance UV–vis spectra of STO, CN, and CN/STO heterojunction photocatalysts. (b) Tauc plots for pure CN and STO used to determine the band gap energy (E_g).

found to be much higher for CN/STO heterojunction compared to pristine CN under both visible and UV light irradiation. Tables 3 and S2 (ESI) summarizes the amount of hydrogen generated by different catalysts in the presence of hole scavenger (triethanolamine, 10% by volume) under visible and UV light irradiations. KSTO, HSTO, and STO do not generate any hydrogen with/or without co-catalyst loading under visible light irradiation ($\lambda \geq 420$ nm) because of their large band gaps. Under UV light irradiation and in the presence of hole scavenger, the amount of hydrogen generated is higher than

the amount generated without hole scavenger (Table S1, ESI). Similarly, the amount of hydrogen produced was found to be higher in the presence of co-catalyst [50].

The amount of hydrogen produced from photocatalytic reduction of water in the presence of STO, CN, and CN/STO with Pt co-catalyst are presented in Fig. 7. As expected, no hydrogen is produced by STO when irradiated by visible light. Under visible light irradiation, the rate of H_2 generation significantly increases from 7.8 µmol/h for CN to 37.2 µmol/h for the CN/STO heterojunction.
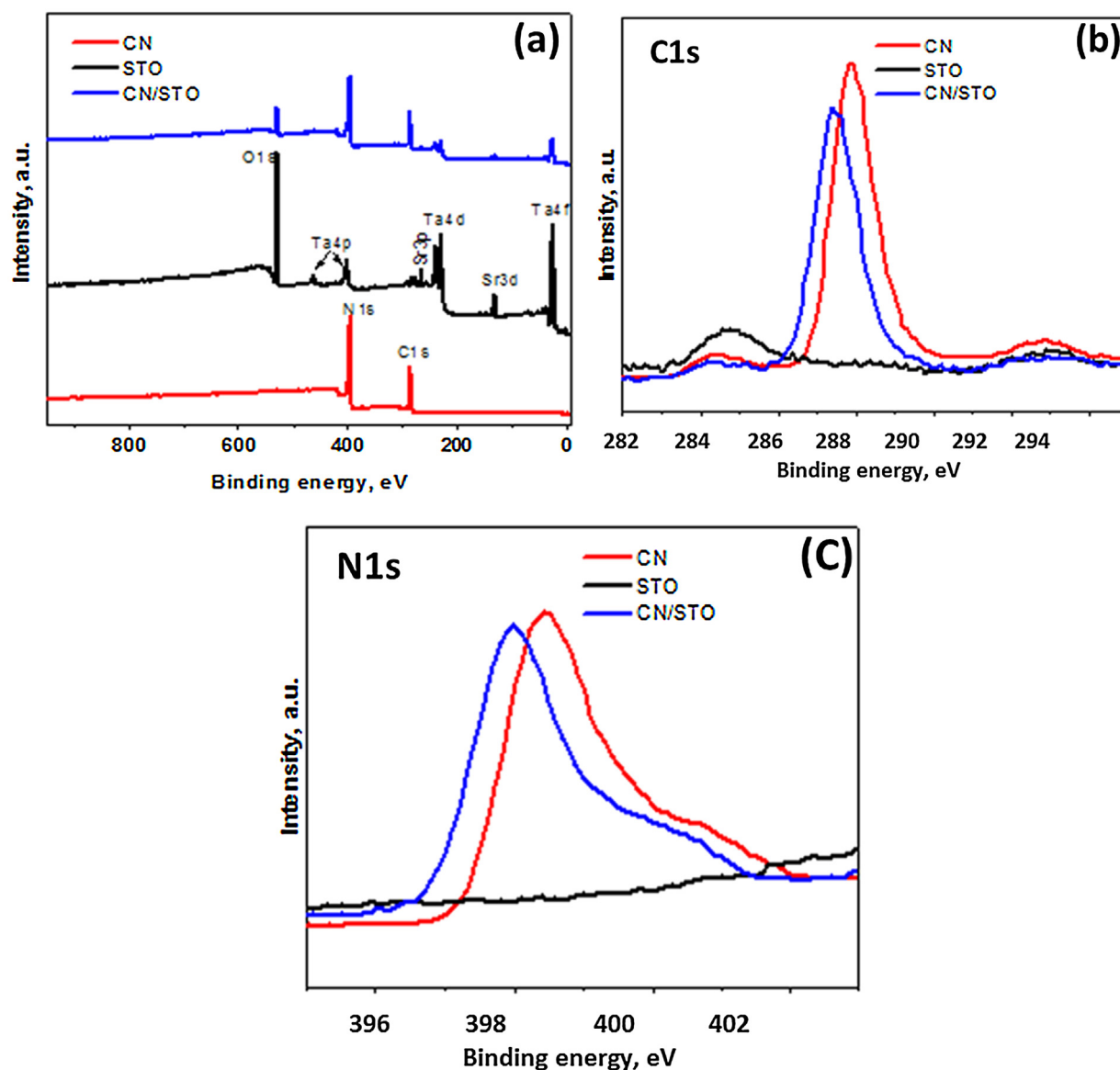
Fig. 6. (a) XPS survey spectrum of CN, STO, and CN/STO heterojunction samples. High-resolution XPS spectra of (b) C 1s, and (c) N 1s.
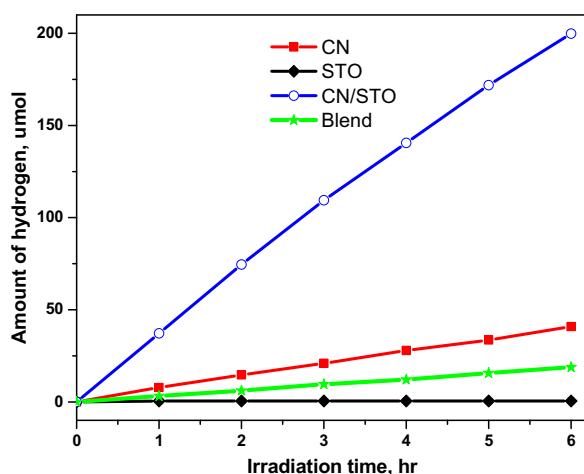

Fig. 7. The rate of hydrogen generation from photocatalytic water reduction under visible light irradiation of STO, CN, CN/STO heterojunction photocatalysts. Conditions: 50 mg catalyst with 2.5 wt.% of Pt cocatalyst, 50 mL 10% vol. triethanolamine aqueous solution, 300 W Xe-lamp with filter for visible light irradiation ($\lambda \geq 420$ nm).

Similarly, the amount of photogenerated hydrogen increases from 8.7 μmol/h to 43.7 μmol/h under UV light irradiation (Table 3). Similar photocatalytic activity studies were performed using physically mixed CN and STO sample (termed "blend sample"). The average hydrogen production rate of the blend was found to be 3.2 μmol/h under visible light irradiation, which is close to that observed for pristine CN. This result confirms that the tight junction between CN and STO in the CN/STO heterojunction allows for better interactions between the two components, which ultimately play an impor-

Table 3

Photocatalytic hydrogen production of different catalysts in the presence of Pt co-catalyst (2.5 wt.%). Conditions: 50 mg catalyst, 50 mL 10% vol triethanolamine aqueous solution, 300 W Xe-lamp. The band pass filter was used to obtain visible light ($\lambda \geq 420$ nm) only.

Sample	UV light, μmol/h	Visible light, μmol/h
KSTO	114	0
HSTO	149	0
STO	10.8	0
CN	8.7	7.8
CN/STO	43.7	37.2

tant role in improving the photocatalytic activity under visible light irradiation.

When exposed to visible-light, the CN/STO heterojunction produces hydrogen at a rate of 137.2 mmol/h/mole of CN (or 811.7 mmol/h/mole of STO), which is ∼9× times larger than the amount of hydrogen generated by one mole of pristine CN. A similar enhancement is observed under UV light (∼10×). This enhancement is superior to that observed for other heterojunctions under similar conditions [26,51–53]. The apparent quantum yields (AQY) were calculated to be 0.35% for CN and 2.62% for the CN/STO heterojunction based on observed activity of 50 mg of the sample for 1 h visible light irradiation (λ = 420 nm). The turnover number (TON) for CN/STO reached ∼2.0 in 15 h with a turnover frequency (TOF) of 0.13. TON and TOF were determined using the amount of hydrogen generated after 15 h of visible light irradiation which was found to be 550 μmol for 50 mg of CN/STO.

To investigate the stability of the CN/STO heterojunction, different runs of water reduction were performed. The amount of hydrogen produced in the third cycle was found to be 177.9 μmol, which is virtually the same amount produced in the first cycle (180.8 μmol), indicating that the heterojunction is stable under visible light irradiation (Fig. S13a, ESI). This is further supported by the PXRD patterns of CN/STO before and after photocatalytic reactions (Fig. S13b, ESI).

3.4. Proposed mechanism

The remarkable activity enhancement of CN/STO heterojunction over pristine CN could be explained on the basis of more efficient charge separation. To elucidate the mechanism of the observed enhanced photocatalytic activity of the CN/STO heterojunction, the relative band positions of the two semiconductors (CN and STO) were determined since band edges play a crucial role in determining the migration pathways of photogenerated charge carriers. The conduction band (CB) bottom (E_{CB}) and valence band (VB) edge (E_{VB}) were calculated empirically using Eqs. (2) and (3) [36,54].

$$E_{CB} = X - 0.5E_g + E_0 \qquad (2)$$

$$E_{VB} = E_{CB} + E_g \qquad (3)$$

Where E_g is the band gap energy of the semiconductor, E_0 is a scale factor relating the reference electrode's redox level to absolute vacuum scale ($E_0 = -4.5$ eV for NHE), and X is the electronegativity of the semiconductor determined as the geometric mean of absolute electronegativities of the constituent atoms. Subsequently, E_{CB} of STO was determined to be −0.59 eV relative to NHE. E_{VB} of STO was calculated to be +3.35 eV based on band gap energy (E_g) of 3.94 eV. Similarly, CB and VB edge potentials for CN were determined to be −1.10 and +1.64 eV, respectively (Fig. 8a). These values were experimentally confirmed by valence band X-ray photoelectron
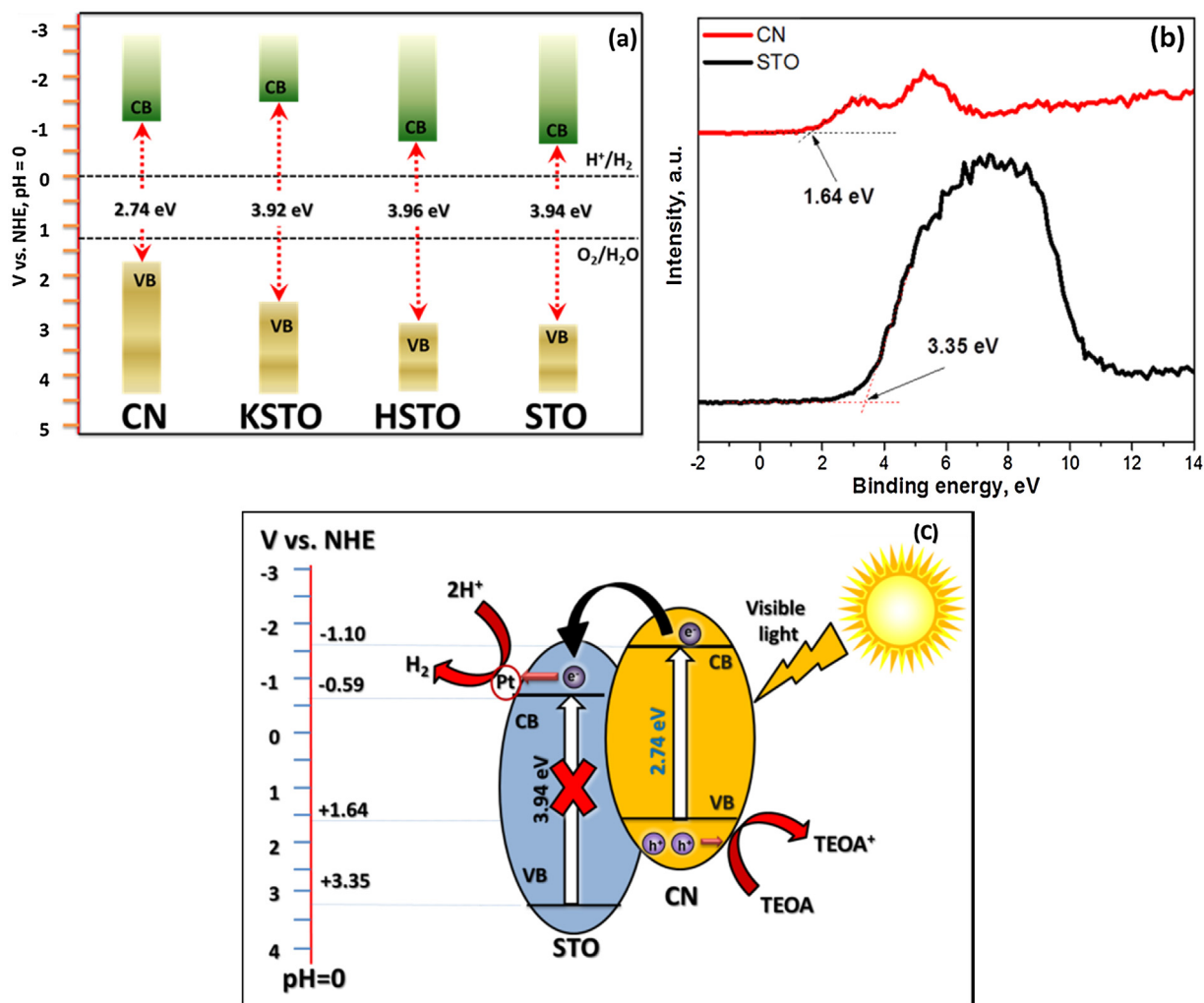

Fig. 8. (a) Relative band positions and band gaps of CN, KSTO, HSTO, and STO. (b) Valence band (VB) XPS spectra of CN and STO (c) Schematic diagram of transfer and separation of photogenerated carriers in CN/STO heterojunction under visible light irradiation.

spectroscopy (VB-XPS) measurements (Fig. 8b). The top of the VB of CN and STO were found to be at +1.64 eV and +3.35 eV respectively, consistent with the calculated values.

As mentioned above, visible light photocatalytic hydrogen production rate of CN/STO heterojunction is much higher than that of CN, which could be ascribed to a good match of CB positions and the synergistic effect between CN and STO as schematically described in the proposed photocatalytic mechanism in Fig. 8c. STO cannot be excited by visible light irradiation because of its large band gap. Thus, photocatalytic hydrogen production by the CN/STO heterojunction can be attributed only to electrons photogenerated from CN. These electrons can transfer to the CB of STO *via* the heterojunction interface since the CB of CN is higher than that of STO. The electrons injected in the CB of STO can then, be transferred to the surface, where they can participate in the reduction of surface adsorbed water molecules to produce hydrogen. On the other hand, photogenerated holes in the VB of CN are trapped by hole scavengers such as triethanolamine (Fig. 8c). Hence, the heterojunction limits the recombination rate of photogenerated electrons, which results in enhanced photocatalytic activity for the CN/STO heterojunction.

To support the above-described mechanism, the lifetime of photogenerated electron-hole pairs was investigated using photo-

luminescence (PL) experiments. High photoluminescence intensity is generally considered to reflect high recombination rate of charge carriers [49,55–57]. The PL emission intensity of the heterojunction CN/STO was found to be significantly smaller compared to that of pristine CN (Fig. 9a), which suggests that the heterojunction has lower recombination rate, consistent with the observed higher photocatalytic activity.

Time-resolved fluorescence emission spectra were collected for CN and CN/STO to determine the lifetime of photogenerated electron-hole pairs in CN and CN/STO (Fig. 9b). The fluorescence intensities for both CN and CN/SNO were best fitted using a tri-exponential curve [58,59]. The weighted average lifetimes (τ_{avg}) were determined to be 64 and 23 ns for CN and CN/STO, respectively (Table 4). The lower lifetime of electrons in CN/STO suggests that electrons in the CB of CN undergo rapid transfer to CB of STO, which presumably improves the separation of charge carriers. This evidence of fast electron injection confirms that the formation of CN/STO heterojunction promotes charge transfer efficiency, thereby favoring photocatalytic water reduction [60,61].

Electrochemical impedance spectroscopy (EIS) was used to determine the migration and transfer rate of photogenerated charge carriers. A smaller arc radius in EIS Nyquist plots corresponds to higher charge carriers mobility [62–64]. The arc diameter
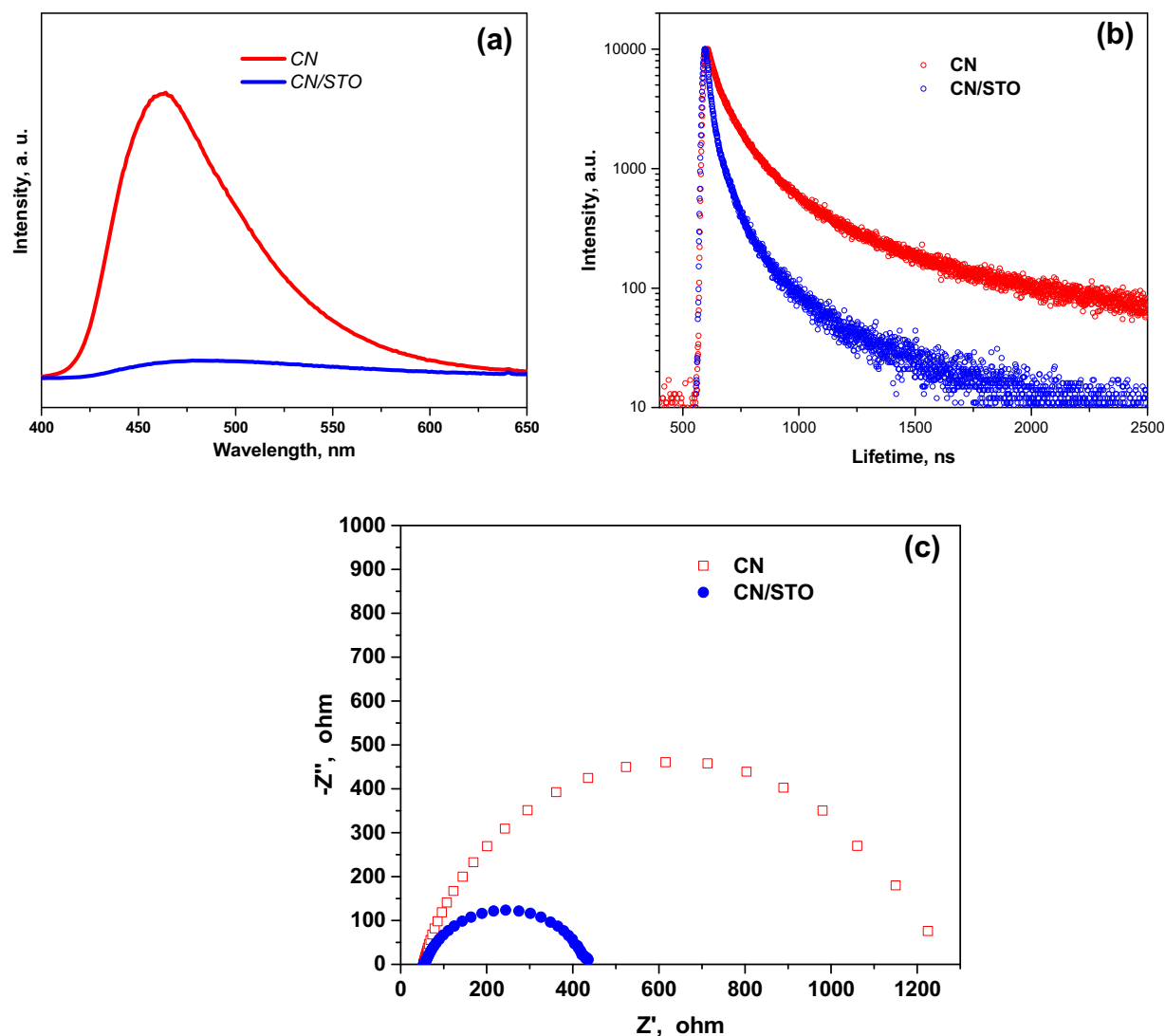

Fig. 9. (a) Photoluminescence (PL) spectra of CN and CN/STO at an excitation wavelength of 336 nm. (b) Time-resolved fluorescence emission decay curves for g-C$_3$N$_4$ and CN/STO. The emission wavelength was set at 460 nm, with the excitation wavelength at 336 nm. (c) EIS of CN and CN/STO.

Table 4
Kinetic parameters of the emission decay for g-C_3N_4 and CN/STO.

Sample	A_1	τ_1 (ns)	A_2	τ_2 (ns)	A_3	τ_3 (ns)	τ_{avg}	χ^2
CN	0.3252	2.4995	0.4271	10.988	0.2477	79.323	64.09	1.315
CN/STO	0.5119	0.7679	0.3695	4.5994	0.1186	33.876	23.60	1.540

for CN was found to be $\sim$1200 Ω, while that of CN/STO is $\sim$400 Ω (Fig. 9c). Thus, the resistance between the CN/STO heterojunction and electrolyte interface is much smaller than that of CN/electrolyte interface. This result revealed that the heterojunction formed between CN and STO would improve the rate of charge transfer by lowering the recombination rate, which is favorable for enhancing the photocatalytic activity of CN in CN/STO heterojunction.

4. Conclusions

In summary, visible-light-active g–C_3N_4/$SrTa_2O_6$ (CN/STO) heterojunction was fabricated using melamine and proton exchanged form ($H_2SrTa_2O_7 \cdot nH_2O$) of $K_2SrTa_2O_7 \cdot nH_2O$ with Ruddlesden-Popper (RP) layered perovskite-type structure. Thermal decomposition of melamine in the presence of $H_2SrTa_2O_7 \cdot nH_2O$ resulted in the formation of a heterojunction composed of metastable strontium tantalate ($SrTa_2O_6$, STO) coated with g-C_3N_4. The heterojunction has strong absorption in the visible light region and possesses significantly enhanced photocatalytic activity towards water reduction. The key to this enhancement relies on proper matching between band positions of CN and STO as well as better separation and transfer of photogenerated electrons at the intimate heterojunction interface.

Acknowledgements

Appendix A. Supplementary data

Supplementary data associated with this article can be found, in the online version, at http://dx.doi.org/10.1016/j.apcatb.2017.05.092.

References

[1] A. Fujishima, K. Honda, Nature 238 (1972) 37–38.
[2] O.A. Ibhadon, P. Fitzpatrick, Catalysts 3 (2013).
[3] A. Mills, S. Le Hunte, J. Photochem. Photobiol. Chem. 108 (1997) 1–35.
[4] F.E. Osterloh, Chem. Soc. Rev. 42 (2013) 2294–2320.
[5] K. Maeda, J. Photochem. Photobiol. C Photochem. Rev. 12 (2011) 237–268.
[6] A.O. Ibhadon, P. Fitzpatrick, Catalysts 3 (2013) 189–218.
[7] C.-H. Liao, C.-W. Huang, J.C.S. Wu, Catalysts 2 (2012) 490–516.
[8] A. Kudo, Y. Miseki, Chem. Soc. Rev. 38 (2009) 253–278.
[9] A. Zaleska, Recent Patents Eng. 2 (2008) 157–164.
[10] M. Ni, M.K.H. Leung, D.Y.C. Leung, K. Sumathy, Renew. Sustain. Energy Rev. 11 (2007) 401–425.
[11] R. Marschall, Adv. Funct. Mater. 24 (2014) 2421–2440.
[12] S.J.A. Moniz, S.A. Shevlin, D.J. Martin, Z.-X. Guo, J. Tang, Energy Environ. Sci. 8 (2015) 731–759.
[13] H. Wang, L. Zhang, Z. Chen, J. Hu, S. Li, Z. Wang, J. Liu, X. Wang, Chem. Soc. Rev. 43 (2014) 5234–5244.
[14] S.P. Adhikari, H. Dean, Z.D. Hood, R. Peng, K.L. More, I. Ivanov, Z. Wu, A. Lachgar, RSC Adv. 5 (2015) 91094–91102.
[15] S.P. Adhikari, Z.D. Hood, K.L. More, I. Ivanov, L. Zhang, M. Gross, A. Lachgar, RSC Adv. 5 (2015) 54998–55005.
[16] C. Xue, T. Zhang, S. Ding, J. Wei, G. Yang, ACS Appl. Mater. Interfaces 9 (19) (2017) 16091–16102.
[17] M. Machida, J. Yabunaka, T. Kijima, Chem. Mater. 12 (2000) 812–817.
[18] M.A. Peña, J.L.G. Fierro, Chem. Rev. 101 (2001) 1981–2018.
[19] A. Kudo, H. Kato, S. Nakagawa, J. Phys. Chem. B 104 (2000) 571–575.
[20] B.V. Beznosikov, K.S. Aleksandrov, Crystallogr. Rep. 45 (2000) 792–798.
[21] T.A. Kodenkandath, J.B. Wiley, Mater. Res. Bull. 35 (2000) 1737–1742.
[22] M.-P. Crosnier-Lopez, F. Le Berre, J.-L. Fourquet, J. Mater. Chem. 11 (2001) 1146–1151.
[23] N.S.P. Bhuvanesh, M.P. Crosnier-Lopez, H. Duroy, J.L. Fourquet, J. Mater. Chem. 9 (1999) 3093–3100.
[24] Y. Zhang, T. Mori, J. Ye, Sci. Adv. Mater. 4 (2012) 282–291.
[25] S. Cao, J. Yu, J. Phys. Chem. Lett. 5 (2014) 2101–2107.
[26] K. Kailasam, A. Fischer, G. Zhang, J. Zhang, M. Schwarze, M. Schröder, X. Wang, R. Schomäcker, A. Thomas, ChemSusChem 8 (2015) 1404–1410.
[27] B. Chai, T. Peng, J. Mao, K. Li, L. Zan, Phys. Chem. Chem. Phys. 14 (2012) 16745–16752.
[28] Y.-P. Zhu, T.-Z. Ren, Z.-Y. Yuan, ACS Appl. Mater. Interfaces 7 (2015) 16850–16856.
[29] S. Guo, Z. Deng, M. Li, B. Jiang, C. Tian, Q. Pan, H. Fu, Angew. Chem. Int. Ed. 55 (2016) 1830–1834.
[30] H. Yan, Chem. Commun. 48 (2012) 3430–3432.
[31] S. Ye, R. Wang, M.-Z. Wu, Y.-P. Yuan, Appl. Surf. Sci. 358 (Part A) (2015) 15–27.
[32] B. Lin, H. An, X. Yan, T. Zhang, J. Wei, G. Yang, Appl. Catal. B Environ. 210 (2017) 173–183.
[33] B. Lin, G. Yang, B. Yang, Y. Zhao, Appl. Catal. B Environ. 198 (2016) 276–285.
[34] Z. Zhao, Y. Sun, F. Dong, Nanoscale 7 (2015) 15–37.
[35] B. Lin, S. Chen, F. Dong, G. Yang, Nanoscale 9 (2017) 5273–5279.
[36] S.P. Adhikari, Z.D. Hood, K.L. More, V.W. Chen, A. Lachgar, ChemSusChem 9 (2016) 1869–1879.
[37] P.J. Ollivier, T.E. Mallouk, Chem. Mater. 10 (1998) 2585–2587.
[38] K. Shimizu, Y. Tsuji, M. Kawakami, K. Toda, T. Kodama, M. Sato, Y. Kitayama, Chem. Lett. 31 (2002) 1158–1159.
[39] J.A. Schottenfeld, Y. Kobayashi, J. Wang, D.D. Macdonald, T.E. Mallouk, Chem. Mater. 20 (2008) 213–219.
[40] Y. Wang, X. Wang, M. Antonietti, Angew. Chem. Int. Ed. 51 (2012) 68–89.
[41] M.A. Rodriguez, T.J. Boyle, B.A. Hernandez, D.R. Tallant, K. Vanheusden, J. Am. Ceram. Soc. 82 (1999) 2101–2105.
[42] Z. Jin, Q. Zhang, S. Yuan, T. Ohno, RSC Adv. 5 (2015) 4026–4029.
[43] A.B. Murphy, Sol. Energy Mater. Sol. Cells 91 (2007) 1326–1337.
[44] S. Chengjie, F. Mingshan, H. Bo, C. Tianjun, W. Liping, S. Weidong, CrystEngComm 17 (2015) 4575–4583.
[45] S. Liang, L. Shen, J. Zhu, Y. Zhang, X. Wang, Z. Li, L. Wu, X. Fu, RSC Adv. 1 (2011) 458–467.
[46] T.L. Barr, S. Seal, J. Vac. Sci. Technol. A 13 (1995) 1239–1246.
[47] C. Han, Y. Wang, Y. Lei, B. Wang, N. Wu, Q. Shi, Q. Li, Nano Res. 8 (2015) 1199–1209.
[48] H. Shi, G. Chen, C. Zhang, Z. Zou, ACS Catal. 4 (2014) 3637–3643.
[49] L. Huang, H. Xu, Y. Li, H. Li, X. Cheng, J. Xia, Y. Xu, G. Cai, Dalton Trans. 42 (2013) 8606–8616.
[50] J. Yang, D. Wang, H. Han, C. Li, Acc. Chem. Res. 46 (2013) 1900–1909.
[51] S.-W. Cao, X.-F. Liu, Y.-P. Yuan, Z.-Y. Zhang, Y.-S. Liao, J. Fang, S.C.J. Loo, T.C. Sum, C. Xue, Appl. Catal. B Environ. 147 (2014) 940–946.
[52] H. Yan, H. Yang, J. Alloys Compd. 509 (2011) L26–L29.
[53] Z. Zhang, K. Liu, Z. Feng, Y. Bao, B. Dong, Sci. Rep. 6 (2016) 19221.
[54] M.A. Butler, D.S. Ginley, J. Electrochem. Soc. 125 (1978) 228–232.
[55] J. Tang, Z. Zou, J. Ye, J. Phys. Chem. B 107 (2003) 14265–14269.
[56] Y. Du, L. Zhao, Y. Zhang, J. Hazard. Mater. 267 (2014) 55–61.
[57] M.T. Mayer, C. Du, D. Wang, J. Am. Chem. Soc. 134 (2012) 12406–12409.
[58] P. Niu, L. Zhang, G. Liu, H.-M. Cheng, Adv. Funct. Mater. 22 (2012) 4763–4770.
[59] S. Nayak, L. Mohapatra, K. Parida, J. Mater. Chem. A 3 (2015) 18622–18635.
[60] Z. Sun, H. Zheng, J. Li, P. Du, Energy Environ. Sci. 8 (2015) 2668–2676.
[61] S.-W. Cao, X.-F. Liu, Y.-P. Yuan, Z.-Y. Zhang, Y.-S. Liao, J. Fang, S.C.J. Loo, T.C. Sum, C. Xue, Appl. Catal. B Environ. 147 (2014) 940–946.
[62] Z. Hosseini, N. Taghavinia, N. Sharifi, M. Chavoshi, M. Rahman, J. Phys. Chem. C 112 (2008) 18686–18689.
[63] X. Bai, L. Wang, Y. Zhu, ACS Catal. 2 (2012) 2769–2778.
[64] B. Hu, F. Cai, T. Chen, M. Fan, C. Song, X. Yan, W. Shi, ACS Appl. Mater. Interfaces 7 (2015) 18247–18256.